Pressure-induced emission enhancement and bandgap narrowing: Experimental investigations and first-principles theoretical simulations on the model halide perovskite $Cs_3Sb_2Br_9$

Debabrata Samanta,[1] Sonu Pratap Chaudhary,[2] Bishnupada Ghosh,[1] Sayan Bhattacharyya,[2] Gaurav Shukla,[3] and Goutam Dev Mukherjee[1,*]

[1]*National Centre for High Pressure Studies, Department of Physical Sciences, Indian Institute of Science Education and Research Kolkata, Mohanpur Campus, Mohanpur 741246, Nadia, West Bengal, India*

[2]*Department of Chemical Sciences, and Centre for Advanced Functional Materials, Indian Institute of Science Education and Research (IISER) Kolkata, Mohanpur 741246, India*

[3]*Department of Earth Sciences and National Centre for High Pressure Studies, Indian Institute of Science Education and Research Kolkata, Mohanpur Campus, Mohanpur 741246, Nadia, West Bengal, India*

(Received 29 September 2021; revised 19 February 2022; accepted 24 February 2022; published 9 March 2022)

We report high-pressure photoluminescence, Raman scattering, and x-ray diffraction measurements on a lead-free halide perovskite $Cs_3Sb_2Br_9$. At about 3 GPa, an electronic transition manifests itself through a broad minimum in linewidth, a maximum in the intensity of E_g, A_{1g} Raman modes, and the unusual change in the c/a ratio of the trigonal lattice. The large compressibility and observed Raman anomalies indicate to a soft material with strong electron-phonon coupling. The observed below-bandgap broadband emission in the photoluminescence measurement indicates the recombination of self-trapped excitons. The initial blueshift of the photoluminescence peak reinforces itself to the redshift at around 3 GPa due to the change in the electronic landscape. A first-order trigonal to a monoclinic structural transition is also seen at 8 GPa. The first-principles density functional theory (DFT) calculations reveal that the electronic transition is associated with direct-to-indirect bandgap transition due to changes in the hybridization of Sb-5s and Br-4p orbitals near the Fermi level in the valence band. The experimentally observed Raman modes are assigned to their symmetry using the density functional perturbation theory. In addition, the DFT calculations predict a 27.5% reduction of the bandgap in the pressure range 0–8 GPa.

DOI: 10.1103/PhysRevB.105.104103

I. INTRODUCTION

The search for energy-efficient materials has gained momentum in recent times, to use with green and renewable energy sources. In this process, the synthesis of the materials with improved efficiency in photovoltaic and optoelectronic properties has generated huge interest in the interdisciplinary field of science. Therefore, it is important to understand not only the fundamental interactions in these materials to predict new novel materials with improved properties but also their behavior under different external conditions. Pressure has been acknowledged as an important clean parameter in this direction. During this search with an emphasis on easy to synthesize and low cost, lead halide perovskites have shown several outstanding properties such as tunable bandgap, large absorption coefficient, low exciton binding energy, high electron and hole mobility leading to good solar material, but the toxicity and poor stability have prevented them from commercial applications [1]. In order to overcome both the toxicity and stability issues, different types of bismuth and antimony-based halide perovskites have been reported. Amongst several candidates, low-toxic antimony and bismuth-based halide perovskites of the family $A_3B_2X_9$ (A: Cs, Rb; B: Sb or Bi; and X: halogen), which are stable under atmospheric conditions have shown good promise [2–9]. The $Cs_3Sb_2Br_9$, a member of the aforementioned family, is a superior candidate for solar cells owing to its direct bandgap, high absorption coefficient ($>10^5$/cm), high photoluminescence quantum yield (PLQY), and small effective mass ($m_e = 0.34$, $m_h = 0.42$) [3–5]. Several studies have been published on $Cs_3Sb_2Br_9$, but mainly focusing on different types of synthesis processes [3,5,9] to improve optoelectronic and photovoltaic properties. The temperature-dependent photoluminescence (PL) study has revealed exciton binding energy of 530 meV and 56.8 meV in the cases of $Cs_3Sb_2Br_9$ QD and $Cs_3Sb_2Br_9$ single crystal, respectively [4,6], showing an important correlation between the structure and optoelectronic properties. But it is noteworthy that the wide bandgap (2.26–2.65 eV) [4–6] of the $Cs_3Sb_2Br_9$ prevents its application in the optoelectronic field. It is extremely difficult to overcome the above issue in a traditional way such as chemical manipulation [10,11] and different processing conditions [3,5,9]. The indirect to direct bandgap transition, enhancement of PLQY, and increase of absorption cross section have been observed by chemical manipulation [12,13]. On the other hand, different processing conditions increase the carrier lifetime [5] and also improve PLQY [9]. Therefore, as mentioned earlier, it is important to analyze and understand the fundamental interactions and the correlation between the structure and the electronic properties.

*Corresponding author: goutamdev@iiserkol.ac.in

To overcome the problem an alternative and efficient way is to use pressure as a parameter and study the physical properties at high densities. Applications of hydrostatic pressure have been found to improve the optical, and the electronic properties of the halide perovskites by tuning interatomic distance without changing the material composition[2,3,14–19]. Application of the pressure on halide perovskites has revealed a variety of pressure-induced phenomena such as structural phase transition [14,16,18], semiconductor to metal transition [2], bandgap optimization [2], emergence of photoluminescence [14,16], crystalline to amorphous transitions [20], etc. The narrowing of the bandgap under pressure is also observed in bismuth and antimony-based halide perovskites. The increase of hybridization of atomic orbitals driven by the reduction of bond length and bridging bond angle leads to narrowing of the bandgap, as seen in zero-dimensional (0D) $Cs_3Bi_2I_9$ [3]. Ting Geng *et al.* have reported a 33.7% reduction in the bandgap under high pressure in two-dimensional (2D) $Cs_3Sb_2I_9$ nanocrystals. Furthermore, first-principles calculations reveal that narrowing of bandgap is driven by the orbital interactions associated with the distortion of the Sb-I octahedral network upon compression [21]. Even after these many studies, the phase stability of bulk $Cs_3Sb_2Br_9$ under pressure, which is important during applications, remains unexplored. Therefore, we have focused on structural, optical, and electronic properties of bulk $Cs_3Sb_2Br_9$ crystal under pressure.

In the present paper, we report a combination of experimental and theoretical studies involving photoluminescence, Raman scattering, powder x-ray diffraction (XRD) measurements, and first-principles calculations as a function of pressure. The $Cs_3Sb_2Br_9$ undergoes two phase transitions upon hydrostatic compression up to about 14 GPa, confirmed by Raman and XRD measurements. An enhancement in PL intensity is observed at 1.4 GPa, which is related to an increase of population of excitons and absorption coefficient at the excitonic energy level with an increase in pressure. In addition, the DFT calculations predict a 27.5% reduction of the bandgap in the pressure range 0–8 GPa.

II. EXPERIMENTAL SECTION

Crystalline powder of $Cs_3Sb_2Br_9$ is prepared by acid precipitation method [14]. High pressure experiments are carried out using a piston-cylinder type diamond anvil cell (DAC) of culet size 300 μm. A steel gasket of thickness 290 μm is preindented to a thickness of 55 μm by squeezing it in between two diamonds and then a 100-μm hole is drilled at the center of the indented portion. The top of the lower diamond together with the central hole of the gasket act as the sample chamber. The sample along with a pressure marker is loaded in the sample chamber. We use 4:1 methanol ethanol mixture as a pressure transmitting medium (PTM) to maintain hydrostatic conditions inside the sample chamber.

High-pressure Raman scattering and PL measurements are carried out using the Raman spectrometer (Monovista from SI GmBH) in the backscattering geometry. 532 nm and 488 nm laser lines are used to excite the sample for Raman and PL experiments, respectively. An infinity-corrected 20X objective is used to focus the incident radiation beam and also to collect the scattered radiations. We have used a few grains of Ruby powder as the pressure marker and the pressure is calculated using the Ruby fluorescence technique [22]. XRD experiments are performed at the XPRESS beamline in the Elettra synchrotron radiation source. A 20 μm diameter monochromatic x-ray of wavelength 0.4957 Å is collimated to the sample for XRD measurements. Pressure is calculated using the equation of state (EOS) of the *Ag* pressure marker [23]. We have employed DIOPTAS software [24] for conversion of 2D diffraction images to intensity versus 2θ plot. All the XRD data are analyzed by CRYSFIRE [25], GSAS [26], and VESTA [27] software. UV-absorption spectrum at ambient conditions is recorded using a Jasco V-670 spectrophotometer.

III. COMPUTATIONAL DETAILS

First-principles density functional theory (DFT) calculations are performed using a plane-wave basis set as implemented in the QUANTUM ESPRESSO [28,29] software. The core and valence electron interactions are described with the ultrasoft pseudopotentials [30]. We have used the ultrasoft pseudopotentials with generalized gradient approximation (GGA) [31] for the calculations of pressure evolution of crystal structure, electronic structure, and phonon modes. The exchange and correlation of electrons are described using Perdew-Burke-Ernzherof (PBE) [31] exchange-correlation functional. A shifted $3 \times 3 \times 2$ Monkhorst-Pack [32] k mesh is chosen for the Brillouin zone summation in the total energy calculations while a shifted, much denser $7 \times 7 \times 6$ k mesh is used for electronic band structure and density of state calculations. The phonon calculations are carried out using the density functional perturbation theory (DFPT) [33]. In phonon density of states calculations, the dynamical matrix is calculated using $2 \times 2 \times 2$ q grid and the obtained force constants are interpolated on a $12 \times 12 \times 12$ q grid. The plane-wave kinetic energy cutoff of 40 Ry and the charge density cutoff of 200 Ry are taken for aforementioned calculations. The k-point grid, kinetic energy cutoff, and charge density cutoff are chosen after a careful convergence test. Structural optimization at each pressure is performed using the variable cell-shape damp dynamic method [34,35] until the magnitude of Hellman-Feynman forces on each atom are smaller than 10^{-5} Ry/a.u. In the case of phonon calculations, the lattice parameters are fixed to their experimental values. Only the internal degrees of freedom are allowed to relax.

IV. RESULTS AND DISCUSSION

A. Experimental

The synthesized $Cs_3Sb_2Br_9$ powder is characterized by synchrotron XRD measurements at ambient conditions. The Rietveld refinement of the XRD pattern at ambient conditions is shown in the Fig. 1(a). The atom positions of $Cs_3Bi_2Br_9$ crystal reported by F. Lazarini [36] are taken as the initial structural model for the Rietveld refinement. The Rietveld refinement of the XRD pattern under the trigonal structure with the space group $P\bar{3}m1$ results in a good fit with the calculated lattice parameters: $a = b = 7.8964(3)$ Å, $c = 9.6989(8)$ Å, which agree well with previously reported literatures [6,37]. The unit cell of $Cs_3Sb_2Br_9$ crystal consists 14 atoms and it is shown in the Fig. 1(b). There is one type of Sb atoms, sitting

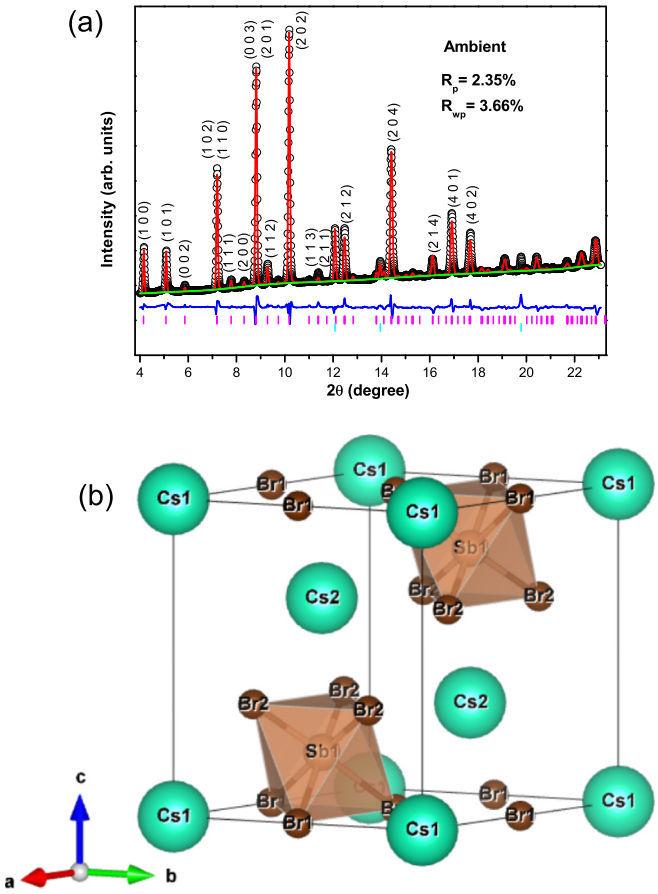

FIG. 1. The Rietveld refinement of the XRD pattern at ambient conditions. The Rietveld refinement shows a good fit with lattice parameters: $a = b = 7.8964(3)$ Å, $c = 9.6989(8)$ Å; space group $P\bar{3}m1$. The black circles are experimental data. The red line shows the Rietveld fit to experimental data. The background is represented by the green line. The blue line shows the difference between experimental and calculated data. The small vertical lines show the Bragg peak of the sample (magenta) and pressure marker(cyan). (b) The unit cell of $Cs_3Sb_2Br_9$ at ambient conditions.

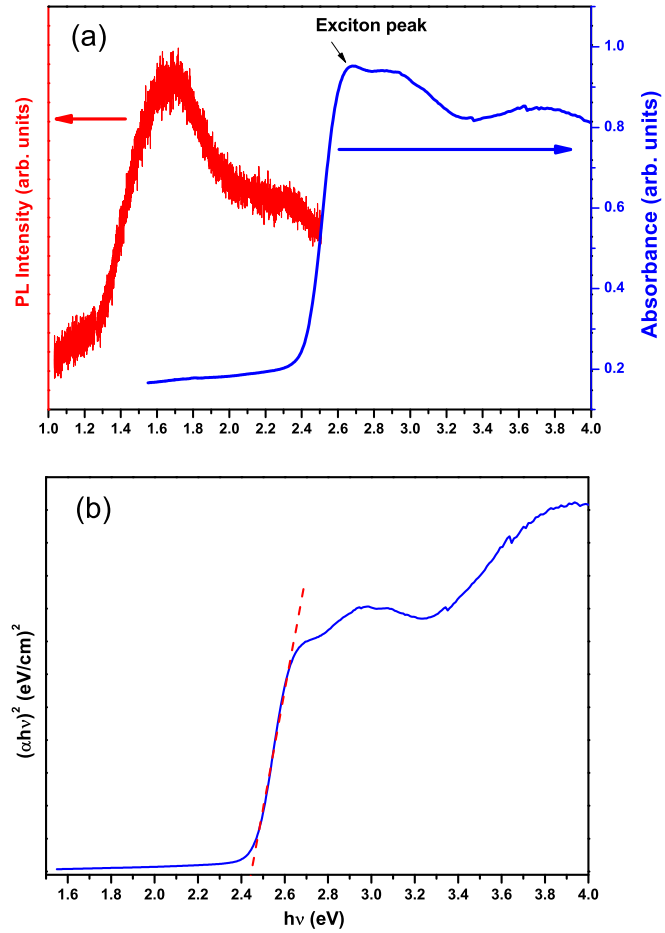

FIG. 2. The PL and absorption spectra of $Cs_3Sb_2Br_9$ at ambient conditions. (b) Tauc's plot of direct bandgap semiconductor $Cs_3Sb_2Br_9$ using UV-visible spectrum at ambient conditions. Tauc's plot method estimates a direct bandgap of 2.45 eV.

at the centers of the $SbBr_6$ octahedra. Two types of Cs atoms are present, which are labeled as Cs1 (occupy the corners of the unit cell) and Cs2 (inside the unit cell). The first type of Br atoms (Br1) occupy Wyckoff position 3e and construct bridges among neighboring octahedra. The second type of Br atoms (Br2), sitting at Wyckoff position 6i participate to form $SbBr_6$ octahedra.

The PL and absorption spectra at ambient conditions are shown in Fig. 2(a). The PL spectrum shows a broad emission centered at around 1.63 eV while an exciton absorption peak is observed at around 2.66 eV. We observe a significant Stokes-shift of about 1.03 eV. Tauc's plot [4] is implemented to estimate the direct optical bandgap of $Cs_3Sb_2Br_9$. The linear portion of $(\alpha h\nu)^2$ *vs* $h\nu$ plot is fitted by the equation: $(\alpha h\nu)^2 = C \times (h\nu - E_g)$; where α is the absorption coefficient, h is Planck's constant, ν is the frequency, C is a proportionality constant, and E_g is the direct optical bandgap. The fit yields $E_g = 2.45$ eV [Fig. 2(b)]. To explore the origin of PL emission, we have performed PL measurements as a function of excitation power at ambient conditions. The PL integrated intensity follows the $I \sim L^K$ law, where L is the excitation power and K is a dimensionless exponent. For exciton (free and/or bound) emission, the K value should be in between $1 < K < 2$ [38]. Our excitation power-dependent-PL analysis reveals a linear behavior with K=1.01 (Fig. S1 within the Supplemental Material [39]). This suggests the excitonic nature of the observed emission. Moreover, the free exciton manifests itself in the PL spectrum with a narrow emission. The observance of broadband emission rules out the possibility of free exciton recombination. In addition, the excitonic emission is usually observed in slightly lower energy than the energy of the bandgap. Furthermore, an unusual type of exciton appears with its broadband emission at much lower energy than the bandgap. This type of exciton is called the self-trapped exciton (STE). Again, the STE emission is a well-known characteristic of the soft halide perovskites with strong electron-phonon coupling strength [40]. Therefore, to confirm the observed emission is an STE recombination or not, detailed pressure-dependent Raman and XRD measurements are needed.

We have recorded high-pressure PL spectra of lead-free halide perovskite $Cs_3Sb_2Br_9$ using an excitation wavelength of 488 nm. Figures 3(a) and 3(b) display PL spectra upon

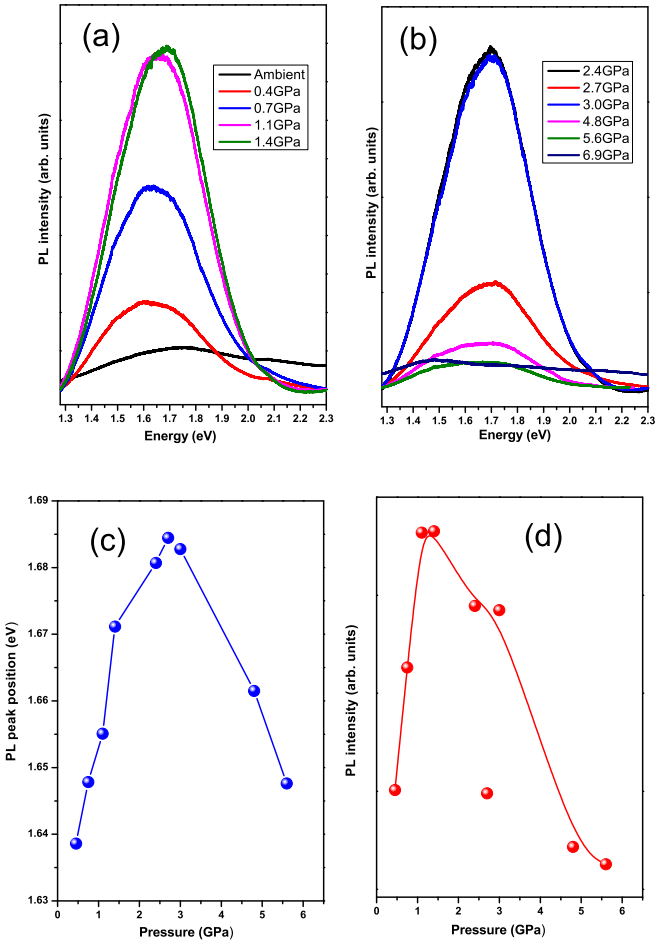

FIG. 3. The pressure evolution of PL spectra of $Cs_3Sb_2Br_9$. The sample is excited with a laser of wavelength 488 nm. (c) PL peak position (d) integrated PL intensity as a function of pressure.

compression at selected pressure points. At ambient conditions, the $Cs_3Sb_2Br_9$ shows a broad emission centered at around 1.63 eV with a long tail on the high energy side. Surprisingly, both the peak position and the intensity show a drastic change with increasing pressure. The PL profile exhibits a maximum in intensity at ∼1.4 GPa. At 6.9 GPa, the PL spectrum shows a broad emission similar to the ambient PL spectrum, but the intensity is found to be lower. To investigate further, the PL spectra are fitted to the Gaussian function. The deconvolution of the PL spectrum at 1.4 GPa is shown in Fig. S2 within the Supplemental Material [39]. The pressure dependence of PL peak position is represented in Fig. 3(c). The PL peak shows a blueshift up to ∼3 GPa followed by a redshift. This may be an indication of a change in crystal and/or electronic structure at ∼3 GPa. As shown in Fig. 3(d), the PL integrated intensity increases up to ∼1.4 GPa followed by a decrease. The decrease of PL integrated intensity may have been caused by an increase in nonradiative processes.

Under ambient conditions, we observe six Raman modes [Fig. 4(a) (bottom panel)], which are labeled as ω_1 (30.2 cm^{-1}), ω_2 (41.1 cm^{-1}), ω_3 (67.4 cm^{-1}), ω_4 (73.3 cm^{-1}), ω_5 (181.8 cm^{-1}), and ω_6 (210.9 cm^{-1}). Three high-frequency Raman modes ω_4, ω_5, and ω_6 agree well with the previously reported Raman spectrum of $Cs_3Sb_2Br_9$ single crystal under ambient conditions [4]. Three low-frequency modes ω_1, ω_2, and ω_3 were not observed in the previous Raman measurements as the experimental frequency range was 50–300 cm^{-1} [4]. We have carried out high-pressure Raman scattering measurements on $Cs_3Sb_2Br_9$ up to around 21 GPa. To extract the pressure dependence of phonon frequencies, linewidth, and intensities, Raman peaks are fitted to Lorentzian functions. Figure 4(a) (top panel) represents Raman spectra of $Cs_3Sb_2Br_9$ at selected pressure points. Upon increasing pressure, all the Raman modes shift towards higher frequency, and eventually, they almost disappear beyond 14 GPa. The observed blueshift of all the Raman modes is related to an increase of bond strength accompanied by the reduction in the interatomic distances. The disappearance of the Raman modes is probably an indication of disordering of the crystal beyond 14 GPa (Fig. S3 within the Supplemental Material [39]). It is also evident from Fig. 4(a) (top panel) that a new mode (ω_7) appears above ∼3 GPa. The pressure behavior of all the Raman mode frequencies are shown in Fig. 4(b). Two low-frequency modes (ω_1, ω_2) show a slope change in their linear pressure behavior at ∼3 GPa and all low-frequency modes merge with the background above 7 GPa. The slope of ω_1 mode is 2.4 cm^{-1}/GPa below 3 GPa and drops to 0.4 cm^{-1}/GPa above 3 GPa. Similarly, the slope of ω_2 is almost two times higher below 3 GPa than that above 3 GPa. In general, the frequency shift of a Raman mode is dominated by anharmonic phonon-phonon interactions. The strong anharmonic phonon-phonon interaction manifests itself through softening of Raman modes with pressure [41,42]. The pressure variation of FWHM of two low-frequency (ω_2, ω_3) and high-frequency (ω_5, ω_6) modes is shown in Fig. 5(a). The contribution of phonon-phonon and electron-phonon interactions decide the phonon life time, which is inversely proportional to the FWHM of Raman mode. Therefore, a study of FWHM with pressure is an indirect way to investigate the pressure dependence of anharmonic phonon-phonon and electron-phonon coupling. Ideally FWHM is expected to increase with an increase in pressure. But we have observed a broad minimum in the pressure range of about 2.5 to 5 GPa. It may be noted that we have used methanol ethanol mixture as a pressure transmitting medium, which preserves the hydrostatic conditions up to about 10 GPa. Hence, the contribution of non-hydrostatic stress to the broadening of Raman modes is completely ruled out. The observed unusual pressure dependence of FWHM for ω_2, ω_3, ω_5, and ω_6 modes is attributed to strong electron-phonon coupling. Therefore, such a broad minimum can be related to either a structural or to an electronic transition in the sample. The variation of the integrated intensity of ω_2, ω_3, ω_5, and ω_6 mode is represented in Fig. 5(b). We see an increase in the integrated intensity by an order of magnitude up to ∼3 GPa. An abrupt increase of the integrated intensity up to ∼3 GPa indicates an enhancement of Raman scattering cross section. In the absence of any change in chemical composition, the enhancement in Raman intensity can be due to a change in the internal polarization of the lattice. This again can happen due to a micro structural reordering. The Raman spectrum regains the original state upon decompression, indicating the reversibility of the disorder phase.

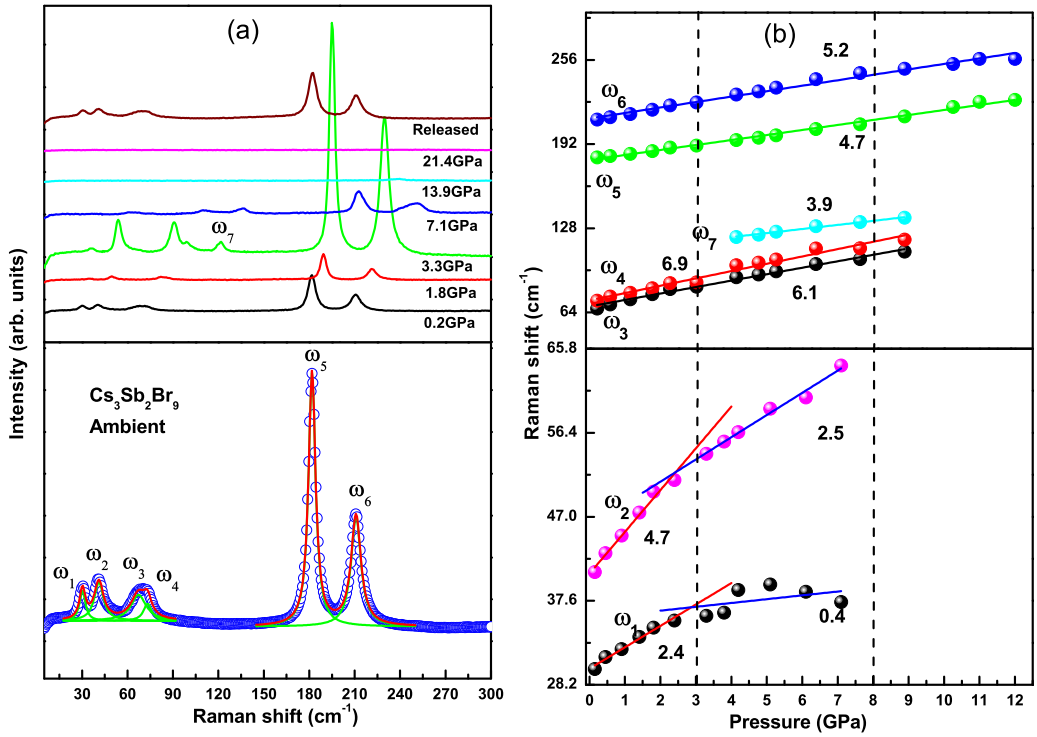

FIG. 4. The deconvolution of the Raman spectrum of $Cs_3Sb_2Br_9$ at ambient conditions. 532 nm laser is used to record Raman spectra under pressure. Blue circles are experimental data. The green lines are the Lorentzian fit to experimental data. The sum of the fit is shown by red lines (bottom panel). Raman spectra of $Cs_3Sb_2Br_9$ at selected pressures (top panel). (b) The pressure dependence of Raman shift of $Cs_3Sb_2Br_9$ crystal. Solid lines represent the linear fit and the slope (in cm^{-1}/GPa) of the linear fit is shown alongside the lines.

To explore further the observed anomalies in the high-pressure Raman analysis, we have performed high-pressure XRD measurements up to ∼20 GPa. All XRD patterns are shown in Fig. S4 within the Supplemental Material [39]. No changes in the XRD patterns are observed up to ∼8 GPa. Drastic changes with the appearance of several new Bragg

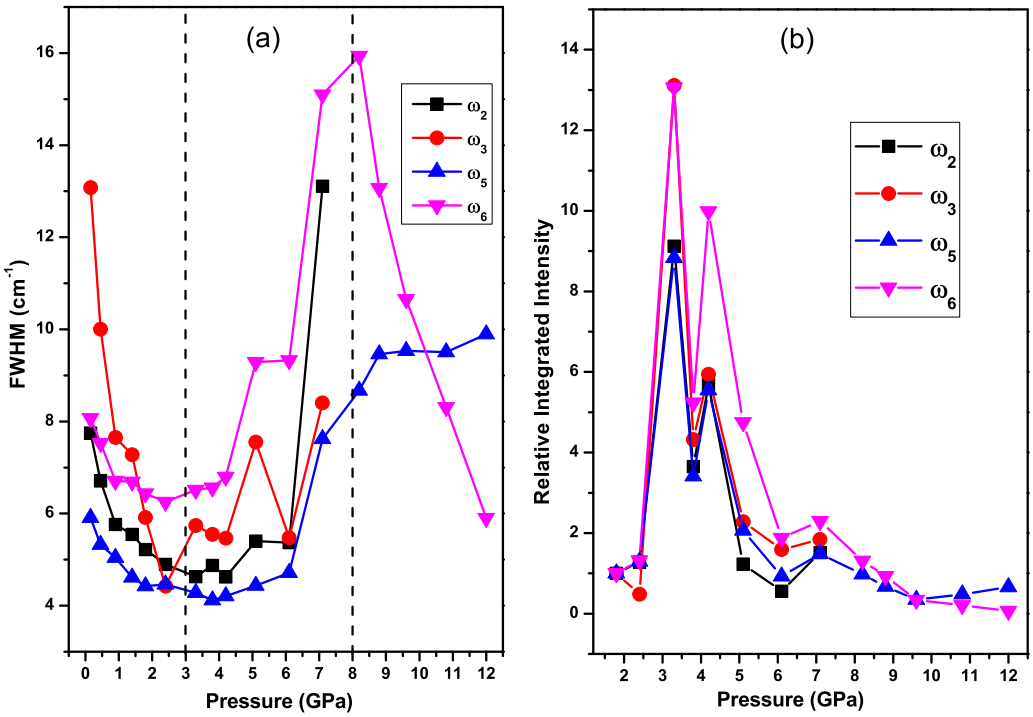

FIG. 5. The variations of (a) FWHM and (b) relative integrated intensity of ω_2, ω_3, ω_5, and ω_6 modes with pressure.

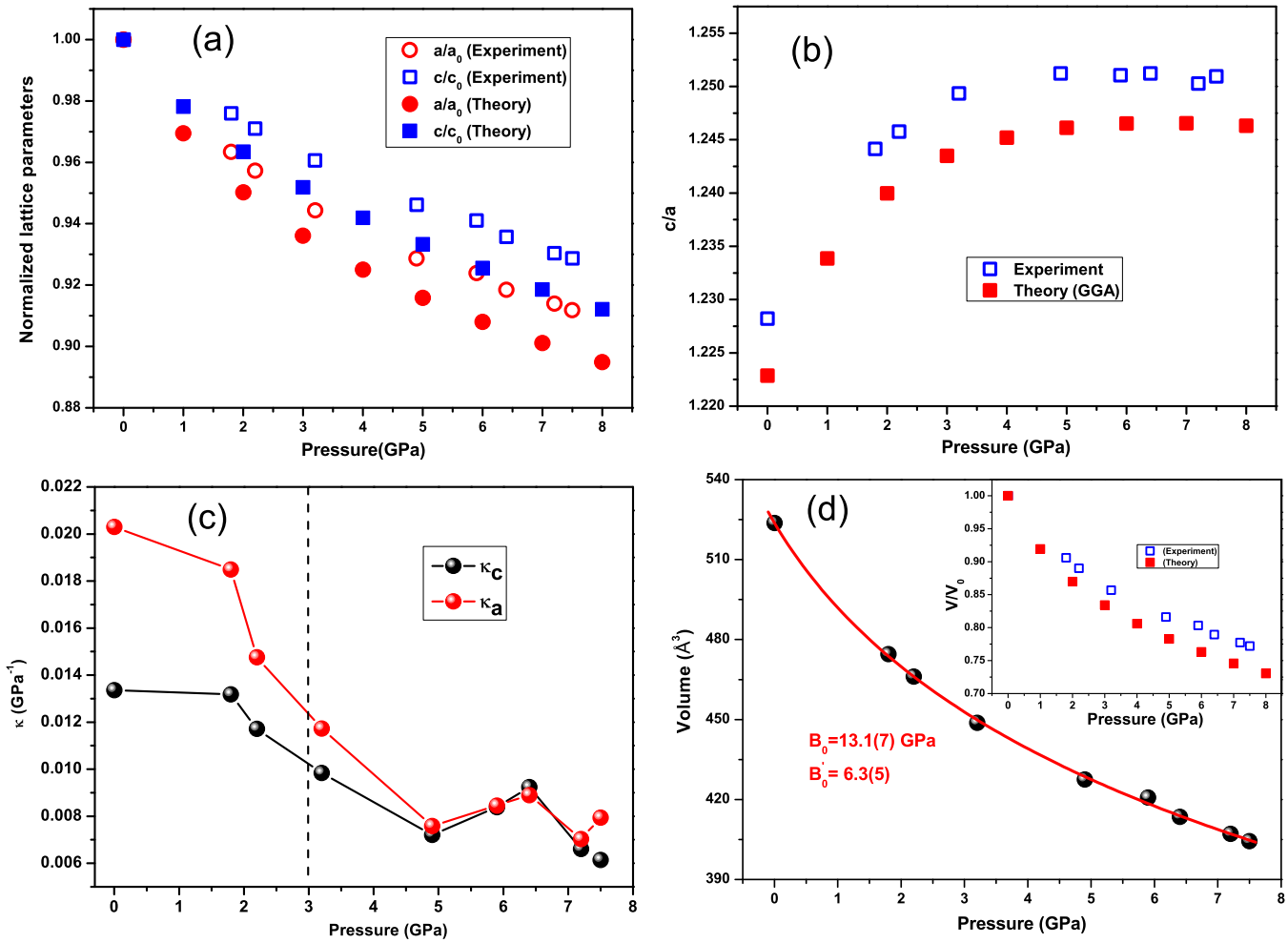

FIG. 6. The figure shows pressure behavior of structural parameters obtained from both theory and experiment. The open circles and the squares are experimental data. The calculated data are shown by the solid circles and the squares. (a) The pressure dependence of the normalized lattice parameters. (b) The change in the c/a ratio as a function of pressure. (c) The variation of liner compressibilities as a function of pressure. (d) The evolution of the cell volume with pressure. The third-order Birch Murnaghan EOS is used to fit the experimental data. The solid line shows the fit. The pressure evolution of the V/V_0 is shown in the inset.

peaks are observed above 8 GPa, suggesting a structural transition. The XRD patterns up to about 8 GPa are analyzed by Rietveld refinements. The evolution of the lattice parameters as a function of pressure [Fig. 6(a)] shows a continuous compression up to ∼8 GPa. However, the c/a ratio as a function of pressure shows an interesting feature [Fig. 6(b)], which increases rapidly up to ∼3 GPa (of the order of about 2%) and then saturates. The c/a ratio in a trigonal lattice can be considered as the strain in the unit cell. The increase of the c/a ratio up to 3 GPa indicates to an increase in the internal strain of the lattice due to the hydrostatic compression. In order to understand the above effect, lattice parameters (a and c) vs pressure data are used to calculate linear compressibility along both a and c-axes. The linear compressibility is defined as $\kappa_{x_i} = -\frac{1}{x_i}\frac{dx_i}{dP}$, where i runs from 1 to 3 ($x_1 = a, x_2 = b, x_3 = c$) and P is the pressure. The evolution of both κ_a and κ_c is shown in Fig. 6(c). κ_a shows a much larger change in comparison to κ_c, up to about 5 GPa indicating anisotropic compressibility. Above 5 GPa, both the axial compressibilities show similar values. It should be noted that the $Cs_3Sb_2Br_9$ is a layered material. A larger change in κ_a indicates a larger compression along the basal plane compared to the prismatic plane and can lead to a micro-structural change in the trigonal lattice. It is noteworthy that a similar anisotropic compressibility has been previously observed in the 0D $Cs_3Sb_2I_9$, and $Cs_3Bi_2I_9$ crystals [2,3]. In Fig. 6(d), we have shown the pressure dependence of volume along with the equation of state (EOS) fit using 3rd order Birch-Murnaghan EOS [23]. Very small value of bulk modulus [$B_0 = 13.1(7)$ GPa] and its large pressure derivative [$B' = 6.3(5)$] indicate an extremely soft lattice. The large compressibility can be related to weaker covalent interaction between Cs^+ and $SbBr_6$. The obtained bulk modulus in the trigonal phase is almost similar to that for $Cs_3Bi_2Br_9$ (12.3 GPa) [14] but about two times smaller than that for 0D $Cs_3Bi_2I_9$ (23.7 GPa) [3] and $Cs_3Sb_2I_9$ (24.7 GPa) [2]. The presence of the soft lattice along with differential compressibility can lead to the overlap of electronic orbitals and an electronic transition. This can be a plausible explanation for the observation of the anomalies in the Raman mode intensity and their band width.

Indexing the XRD pattern at 9.3 GPa reveals a monoclinic structure with structural parameters: $a = 9.0515(7)$ Å,

TABLE I. A list of optimized lattice parameters and their experimental values at ambient conditions.

Approximation	Lattice parameters	Experiment (Å)	Theory (Å)	Error in %
GGA	a	7.8964	8.1334	3
	c	9.6989	9.9460	2.5

$b = 7.6480(8)$ Å, $c = 10.7902(11)$Å, $\beta = 105.709(8)^{o}$; space group: $P21/n$. In the absence of any structural model, we have carried out the Le-Bail profile refinement of the XRD pattern at 9.3 GPa as shown in Fig. S5(b) within the Supplemental Material [39]. The pressure dependence of lattice parameters (Fig. S6 within the Supplemental Material [39]) exhibits a nonlinear behavior. Moreover, the monoclinic structure preserves up to ∼13 GPa. At 15.3 GPa, a diffuse background in the 2θ range 9–12 degrees along with few broad Bragg peaks appear indicating that the sample crystallinity begins to deteriorate and it continues up to 20 GPa, the highest pressure of our experiments. The EOS fit gives $B_0 = 99.5(1)$ GPa, $B' = 10.0(3)$ for the monoclinic phase, which is much larger than that for the trigonal phase. The discontinuity in volume vs pressure data ∼8 GPa confirms that the observed trigonal to monoclinic structural transition is first-order in nature.

B. Theory

To understand the observed Raman anomalies and the interesting feature in the c/a ratio ∼3 GPa, the first-principles calculations as a function of pressure are employed for the trigonal phase. The optimized lattice parameters along with their experimental values are represented in Table I. The optimized lattice parameters agree well with our experimental lattice parameters within the typical error of DFT calculations. The GGA overestimates the lattice parameters. However, we put more emphasis on the variation of the normalized lattice parameters $(a/a_0, c/c_0)$ with pressure, where a_0, c_0 are the lattice parameters at ambient pressure. The calculated pressure behavior of the normalized lattice parameters is consistent with our experimental results as shown in Fig. 6(a). Our DFT calculations predict the unit cell volume to be 569.8 Å^3 while the unit cell volume of 523.7 Å^3 is calculated from the XRD analysis, an overestimation of about 9%. The evolution of the calculated c/a ratio as a function of pressure is compared with the experimental data in Fig. 6(b), which is well reproduced. The normalized unit cell volume obtained from both theory and experiment follows a similar trend with increasing pressure [inset of Fig. 6(d)]. The third-order Brich Murnaghan EOS is used to fit the computed volume vs pressure data (Fig. S7 within the Supplemental Material [39]). The fit estimates the bulk modulus to be 10.9 GPa (The bulk modulus of 13.1 GPa is estimated from the experiment). The GGA calculations underestimate the bulk modulus by about 16.8%. The discrepancy in the bulk modulus is frequently observed in DFT [43–46]. Bulk modulus is in close relation with unit-cell volume. Therefore, the discrepancy in the bulk modulus can be correlated to error introduced in the unit-cell volume.

TABLE II. A list of experimental and calculated Raman mode frequencies at ambient conditions.

Experimental frequencies		Calculated frequencies	
Mode	Mode frequency cm^{-1}	Mode symmetry cm^{-1}	Mode frequency
ω_1	30.2	E_g	28.3
ω_2	41.1	E_g	36.4
ω_3	67.4	A_{1g}	38.5
ω_4	73.3	A_{1g}	66.5
ω_5	181.8	E_g	69.3
ω_6	210.9	E_g	85.1
		A_{1g}	102.5
		E_g	176.2
		A_{1g}	203.5

The $Cs_3Sb_2Br_9$ crystal with space group $P\bar{3}m1$ (D_{3d}) contains 14 atoms per unit cell. The group theory analysis predicts 42 vibrational modes at zone center, which are represented as $\Gamma_{vib} = A_{2g} + 2A_{1u} + 4A_{1g} + 5E_g + 7A_{2u} + 9E_u$. Where A_{1g}, E_g modes are Raman active and A_{2u}, E_u are IR-active modes. E_g and E_u are double-degenerate modes. Therefore, in the Raman spectrum, we can expect nine distinct Raman active modes ($4A_{1g} + 5E_g$) (Table II). The nine Raman active modes are calculated to be: A_{1g} (203.5 cm^{-1}), E_g (176.2 cm^{-1}), A_{1g} (102.5 cm^{-1}), E_g (85.1 cm^{-1}), E_g (69.3 cm^{-1}), A_{1g} (66.5 cm^{-1}), A_{1g} (38.5 cm^{-1}), E_g (36.4 cm^{-1}), and E_g (28.3 cm^{-1}). The visualization of the displacements of atoms associated with each modes are shown in Fig. 7. The A_{1g} modes at 203.5 cm^{-1} and 102.5 cm^{-1} originate due to symmetric vibration of $SbBr_6$ octahedra. The vibrations of the octahedra are accompanied by the displacement of both Sb and Br2 atoms. The displacements of the Sb atoms are along the c-axis, for both the A_{1g} modes at 203.5 cm^{-1} and

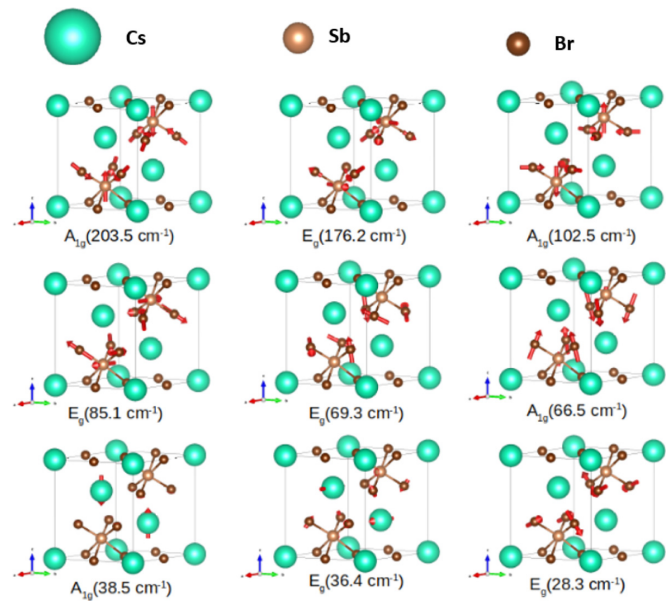

FIG. 7. Visualization of the atomic displacements of the selected Raman modes obtained from DFPT calculations.

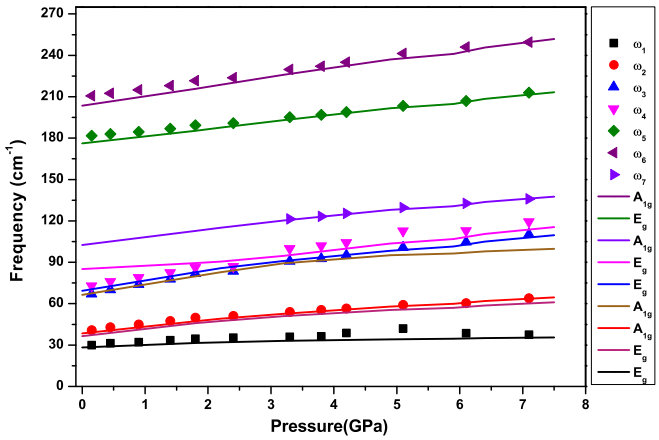

FIG. 8. The pressure variation of Raman mode frequencies of $Cs_3Sb_2Br_9$ from DFT calculations and experiment. The points are experimental data. The calculated data are shown by solid lines.

102.5 cm^{-1}. E_g modes at 176.2 cm^{-1} and 85.1 cm^{-1} are assigned to asymmetric vibration of $SbBr_6$ octahedra. Both Sb and Br2 atoms take part in the asymmetric vibrations. The displacements of the Sb atoms for both the E_g modes at 176.2 cm^{-1} and 85.1 cm^{-1} are in the $a-b$ plane. The E_g mode at 69.3 cm^{-1} and A_{1g} mode at 66.5 cm^{-1} are associated with the symmetric and the asymmetric vibrations of $SbBr_6$ octahedra, respectively. The vibrations of the $SbBr_6$ octahedra are contributed by Br2 atoms only. Mostly, the vibrations of Cs2 atoms in the $a-b$ plane and perpendicular to the $a-b$ plane are attributed to E_g mode at 38.5 cm^{-1} and A_{1g} mode at 36.4 cm^{-1}, respectively. The E_g mode at 28.3 cm^{-1} mainly originates due to the rotation of $SbBr_6$ octahedra.

Our DFT calculations predict nine distinct Raman active modes but experimentally we observe only six Raman modes at ambient conditions (Table II). Two observed high-frequency modes ω_5 (181.8 cm^{-1}), ω_6 (210.9 cm^{-1}) are assigned to calculated phonon modes E_g (176.2 cm^{-1}), A_{1g} (203.5 cm^{-1}), respectively. The calculated A_{1g} (102.5 cm^{-1}) mode can be related to the observed ω_7 mode, which appeared beyond 3 GPa. The non-observance of ω_7 mode at ambient conditions can be attributed to weak Raman scattering cross-section. The observed low frequency modes are very close to each other, therefore it is difficult to identify each mode separately. However, we make a comparison between the calculated and the observed modes in the low-frequency region. Two observed ω_3 (67.4 cm^{-1}), ω_4 (73.3 cm^{-1}) modes can be compared to E_g (85.1 cm^{-1}), E_g (69.3 cm^{-1}), and A_{1g} (66.5 cm^{-1}). The experimentally observed ω_2 (41.1 cm^{-1}) mode can be assigned to either A_{1g} (38.5 cm^{-1}) or E_g (36.4 cm^{-1}). The observed ω_1 (30.2 cm^{-1}) mode is identified to E_g (28.3 cm^{-1}) symmetry.

The pressure evolution of Raman mode frequencies obtained from both experiments and calculations is shown in Fig. 8. The pressure variation of the calculated modes agrees well with our experimental results. The phonon density of states at selected pressure values are presented in Fig. S8 within the Supplemental Material [39]. The phonon density of states spreads to a higher frequency with increasing pressure. The absence of the phonon density of states in the negative

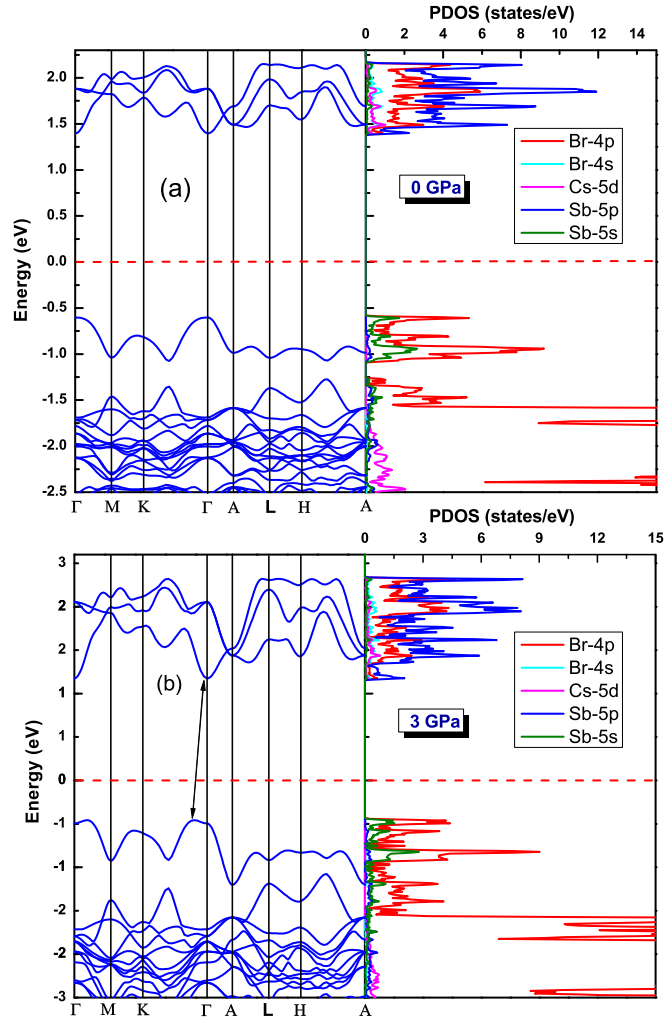

FIG. 9. The Electronic band structure and projected electronic density of states at 0 GPa. (b) The Electronic band structures and projected electronic density of states at 3 GPa. The arrow in the band structure is showing the direct to indirect bandgap transition.

frequency indicates the stability of the structure up to ~8 GPa and no obvious anharmonic phonon-phonon interactions. The calculated results are in good agreement with the results obtained from Raman scattering measurements.

The band structure of $Cs_3Sb_2Br_9$ at 0 GPa is displayed in Fig. 9(a). It is seen that the direct bandgap occurs at Γ point and is found to be 2 eV. The calculated bandgap value is underestimated by 18%. This is a well-known drawback of standard DFT calculations with GGA [47], even though it captures the correct pressure variation of the bandgap. Some sophisticated functionals, such as mBJ, HLE16, and HSE06 can predict accurate bandgap [47]. However, we avoided band structure calculations using these functional due to high computational costs. It should be noted that the band structure calculation using HSE06 predicts the bandgap to be 2.6 eV [48]. The bandgap of 1.4 eV and 2.07 eV are predicted by DFT calculation using PBEsol, and HSE06 functional with taking into account the spin-orbit coupling (SOC) effect, respectively [49]. The $Cs_3Sb_2Br_9$ has a direct optical bandgap in the range 2.26–2.65 eV [4–6] and it is calculated from the

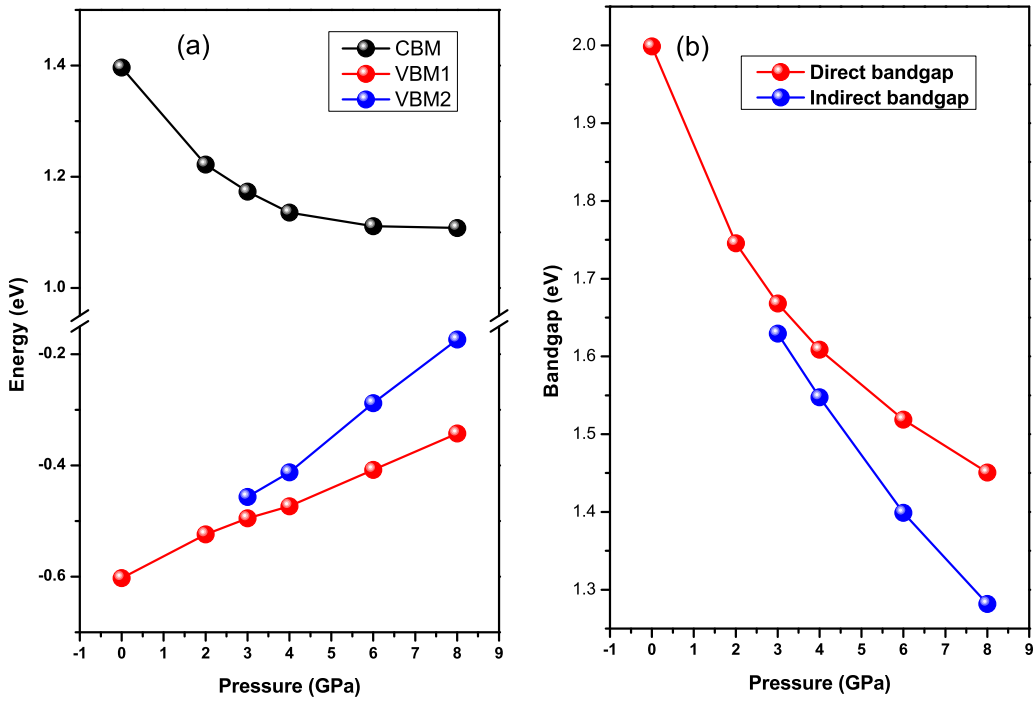

FIG. 10. The pressure evolution of the VBM and CBM. (b) The evolution of both the direct and indirect bandgaps as a function of pressure.

absorption spectrum. The estimated direct bandgap (2.45 eV) in the present work also belongs to the same range. To shed light on orbital characteristics of the conduction and valence band, we have calculated the projected density of states (PDOS) at different pressures. As shown in Fig. 9(a), at ambient pressure the strong $p-p$ interactions throughout the conduction band are accompanied by the hybridization of $\mathrm{Sb}-5p$ and $\mathrm{Br}-4p$ atomic orbitals. On the other hand, typical $s-p$ interactions from hybridization of $\mathrm{Br}-4p$ and $\mathrm{Sb}-5s$ atomic orbitals are present throughout the valence band. The electronic band structures and PDOS at selected pressure are shown in Fig. S9 and Fig. S10 (within the Supplemental Material [39]), respectively. The electronic band structure calculations as a function of pressure reveal a direct to indirect bandgap transition at 3 GPa [Fig. 9(b)]. The indirect bandgap occurs at Γ point to a low-symmetry point along Γ-to-K direction as shown by an arrow in Fig. 9(b). At 3 GPa, as shown in Fig. 9(b), the conduction band is dominated by strong hybridizations of $\mathrm{Sb}-5p$ and $\mathrm{Br}-4p$ atomic orbitals whereas the valence band is mostly associated with the hybridization of $\mathrm{Br}-4p$ and $\mathrm{Sb}-5s$ orbitals. The conduction band minimum (CBM) and valence band maximum (VBM) at Γ point are denoted by CBM and VBM1, respectively. The VBM at slightly off Γ (Γ-to-K direction) is denoted by VBM2. The CBM shows a sharp decreasing tendency up to 3 GPa followed by a pressure invariant behavior, while VBM1 and VBM2 increase monotonically with increasing pressure [Fig. 10(a)]. The CBM plays a leading role up to ∼3 GPa, and beyond that pressure, VBM1 and VBM2 play the leading role in the bandgap narrowing. However, the cumulative pressure behavior of CBM, VBM1, and VBM2 results in a decrease of both direct and indirect bandgap [Fig. 10(a)]. The pressure evolution of both direct and indirect bandgaps are displayed in Fig. 10(b). Both direct and indirect bandgaps are found to decrease monotonically with increasing pressure. Moreover, the DFT calculations predict a 27.5% reduction of the bandgap in the pressure range 0–8 GPa.

We have partially assigned Raman modes of the $Cs_3Sb_2Br_9$ crystal based on our experimental and theoretical studies. Polarized Raman measurements on single crystals can provide accurate Raman mode assignment. Noting that low-frequency modes of $Cs_3Sb_2Br_9$ have low intensity and are very close to each other. Therefore, the assignments of these modes are extremely difficult by polarized Raman measurements at ambient conditions. In that case, the polarized Raman measurement at low temperature could provide an accurate assignment of Raman modes, which is beyond the scope of our experimental study. The electron-phonon interactions and anharmonic phonon-phonon interactions contribute to the phonon linewidth. The anharmonic phonon-phonon interactions do not contain any information about the electronic band since it is independent of carrier density [50]. We do not observe any soft mode in theory as well as in experiment (Fig. S8 within the Supplemental Material [39]). The contribution of electron-phonon interactions to phonon linewidth comes from the scattering rate of phonons by charge carriers. This rate can be calculated from the imaginary part of the phonon self-energy. The Raman linewidth is directly related to the electronic density of state and electronic band involved in the electron-phonon matrix element [50,51]. Therefore, any changes in the electronic band structure will be reflected in the FWHM of the Raman mode. The observed broad minimum in FWHM of ω_2, ω_3, ω_5, and ω_6 modes ∼3 GPa is attributed to electron-phonon coupling associated with direct-to-indirect bandgap transition, as evidenced by our electronic band structure calculations. The CB and VB are mostly associated with

strong $p-p$ and $s-p$ interactions of Sb and Br atoms, respectively. Therefore, it is correlated that the $SbBr_6$ octahedra volume contraction takes part in the narrowing of the bandgap. The pressure-dependent XRD and Raman study jointly reveal the $Cs_3Sb_2Br_9$ crystal to be a soft (low bulk modulus) material with strong electron-phonon coupling. The soft material having strong electron-phonon interactions is conducive to form the self-trapped states. Hence, the observed below bandgap broad emission in the PL measurements is attributed to the phonon-assisted recombination of self-trapped excitons [3,14,40,52]. The population of excitons and absorption coefficient at the excitonic energy level increase with increasing pressure, which leads to an increase in PL intensity up to around 1.4 GPa [53]. The PL peak blueshifts with pressure by about 0.06 eV in the 0–3 GPa range. In a high pressure study on a halide double perovskite $Cs_2AgBiCl_6$, Zhang *et al.* have observed a blueshift in PL peak value, even though there is a reduction in bandgap in the same pressure range and have explained the blueshift in the PL peak by the reduction in the lattice relaxation energy [54]. One can model the PL emission in the present case using the configurational coordinate model of phonon-assisted STE recombination, which depends strongly on the electron-phonon coupling [55]. The broad shape of the PL band is attributed to strong electron-phonon coupling which leads to charge localization and emission of phonons that alter the energy of the emitted photon. The XRD data show an increase in c/a ratio till about 3 GPa followed by a saturation, indicating stabilization of lattice strain above 3 GPa. Raman data show an enhancement of Raman intensity at about 3 GPa and a minimum in the FWHM of the Raman modes at the same pressure indicating a maximum in lifetime of phonon modes at 3 GPa. These results indicate a reduction in anharmonic multiphonon scattering at the same pressure. Interestingly, the FWHM of PL band shows a minimum at 3 GPa (Fig. S11 within the Supplemental Material [39]), indicating reduction of multiphonon scattering process. Therefore, in all possibility the STE emission is less affected by anharmonic multiphonon processes and hence there is a slight blue shift of the PL peak up to 3 GPa. Our DFT calculations show the direct band gap decreases by about 17.5% up to about 3 GPa. Even though the DFT calculations underestimate the band gap value, it is well known that it captures the change with pressure quite accurately. Therefore, by considering the decrease of about 17.5% in the bandgap, the actual bandgap can be estimated to be about 2.03 eV (considering 2.45 eV at ambient pressure). The PL peak is at 1.69 eV at 3 GPa, which is lower than the conduction band edge. Therefore, the blue shift can be related to the reduction in the anharmonic multiphonon scattering process due to stabilization of internal lattice strain. Red shift in the PL peak above 3 GPa and reduction in the PL intensity can be related to the direct to indirect band transition. Our calculations suggest that the direct bandgap redshifts by about 0.6 eV from 0 to 6 GPa. Therefore, the optical direct bandgap of 2.45 eV at ambient pressure would move to 1.85 eV at 6 GPa, which indicates that the exciton peak may shift from 2.66 eV to 2.06 eV in the same pressure range. The STE emission peak is observed at 1.65 eV at around 6 GPa, leading to a stokes shift of about 0.4 eV. We believe that above 6 GPa, possibly the stokes shift reduces further due to the reduction in the bandgap. We have observed extensive broadening of Raman modes above 6 GPa indicating an increase in disorder in the parent trigonal structure, which possibly acts as a precursor to the structural transition at 8 GPa. All these effects including the direct to indirect bandgap transition are probably responsible for drastic reduction of STE emission beyond 6 GPa. Due to the decrease in the bandgap, there would be an intermediate pressure at which the laser line at 532 nm (2.33 eV) used for Raman experiments will coincide with optical bandgap. At around 3GPa, we have observed a sudden increase in Raman intensity and we have earlier argued due to an electronic transition. The coincidence of photon energy with the optical bandgap may result in a resonance condition, which can lead to the enhancement of the Raman intensity. All the above results highlight how the optical response is modified by the ability to contract a crystal in a particular direction.

V. CONCLUSIONS

We have investigated an electronic transition associated with direct-to-indirect bandgap transition ∼3 GPa from both experiments and first-principle density functional theory calculations. High-pressure Raman measurements show a broad minimum in linewidth of A_{1g} and E_g modes at ∼3 GPa due to unusual electron-phonon coupling. A larger compression along the basal plane compared to the prismatic plane leads to a micro-structural change in the trigonal lattice, as evidenced from XRD analysis. Self-trapped exciton manifests itself in the photoluminescence spectra through below bandgap broadband emission and the emission gets enhanced under pressure. The DFT calculation reveals that the electronic transition is associated with direct-to-indirect bandgap transition. Intriguingly, a 27.5% narrowing of the bandgap is estimated by the first-principles calculations within the GGA to an electronic exchange and correlation functional. Furthermore, our paper not only provides a relationship between optical properties and structural evolution of the $Cs_3Sb_2Br_9$ under pressure but also shows an effective way for achieving high optical response by tuning interatomic distances without changing the material composition. We also believe that this paper will influence further research to understand the peculiarity of property-structure relation of the lead-free halide perovskites.

ACKNOWLEDGMENTS

We acknowledge the financial support from the Ministry of Earth Sciences, Government of India, Grant No. MoES/16/25/10-RDEAS. The financial support from Department of Science and Technology, Government of India under Indo-Italy Executive Programme of Scientific and Technological Cooperation is gratefully acknowledged. The XRD measurements are carried out in the spare time of the Proposal ID 20190546. D.S. also acknowledges the Fellowship Grant supported by the INSPIRE program, Department of Science and Technology, Government of India.

[1] W. Zhang, G. E. Eperon, and H. J. Snaith, Nat. Energy **1**, 16048 (2016)

[2] L. Wu, Z. Dong, L. Zhang, C. Liu, K. Wang, and B. Zou, ChemSusChem **12**, 3971 (2019)

[3] L. Zhang, C. Liu, L. Wang, Ca. Liu, K. Wang, and B. Zou, Angew. Chem. Int. **57**, 11213 (2018)

[4] P. Liu, Y. Liu, S. Zhang, J. Li, C. Wang, C. Zhao, P. Nie, Y. Dong, X. Zhang, S. Zhao, and G. Wei, Adv. Opt. Mater. **8**, 2001072 (2020)

[5] Z. Zheng, Q. Hu, H. Zhou, P. Luo, A. Nie, H. Zhu, L. Gan, F. Zhuge, Y. Ma, H. Song, and T. Zhai, Nanoscale Horiz. **4**, 1372 (2019)

[6] J. Zhang, Y. Yang, H. Deng, U. Farooq, X. Yang, J. Khan, J. Tang, and H. Song, ACS Nano **11**, 9294 (2017)

[7] S. F. Hoefler, G. Trimmel, and T. Rath, Mon. Chem. **148**, 795 (2017)

[8] B. Pradhan, G. S. Kumar, S. Sain, A. Dalui, U. K. Ghorai, S. K. Pradhan, and S. Acharya, Chem. Mater. **30**, 2135 (2018)

[9] Z. Ma, Z. Shi, D. Yang, F. Zhang, S. Li, L. Wang, D. Wu, Y. Zhang, G. Na, L. Zhang *et al.*, ACS Energy Lett. **5**, 385 (2020)

[10] Q. A. Akkerman, V. D'Innocenzo, S. Accornero, A. Scarpellini, A. Petrozza, M. Prato, and L. Manna, J. Am. Chem. Soc. **137**, 10276 (2015)

[11] D. Manna, J. Kangsabanik, T. K. Das, D. Das, A. Alam, and A. Yella, J. Phys. Chem. Lett. **11**, 2113 (2020)

[12] B. Yang, X. Mao, F. Hong, W. Meng, Y. Tang, X. Xia, S. Yang, W. Deng, and K. Han, J. Am. Chem. Soc. **140**, 17001 (2018)

[13] J. Luo, X. Wang, S. Li, J. Liu, Y. Guo, G. Niu, L. Yao, Y. Fu, L. Gao, Q. Dong *et al.*, Nature (London) **563**, 541 (2018)

[14] D. Samanta, P. Saha, B. Ghosh, S. P. Chaudhary, S. Bhattacharyya, S. Chatterjee, amd G. D. Mukherjee, J. Phys. Chem. C **125**, 3432 (2021)

[15] Y. Nagaoka, K. Hills-Kills, R. Tan, R. Li, Z. Wang, and O. Chen, Adv. Mater. **29**, 1606666 (2017)

[16] Z. Ma, Z. Liu, S. Lu, L. Wang, X. Feng, D. Yang, K. Wang, G. Xiao, L. Zhang Simon A. T. Redfern and B. Zou, Nat. Commun. **9**, 4506 (2018)

[17] C. Lv, X. Yang, Z. Shi, L. Wang, L. Sui, Q. Li, J. Qin, K. Liu, Z. Zhang, X. Li *et al.*, J. Phys. Chem. C **124**, 1732 (2020)

[18] R. Fu, Y. Chen, X. Yong, Z. Ma, L. Wang, P. Lv, S. Lu, G. Xiao, and B. Zou, Nanoscale **11**, 17004 (2019)

[19] Q. Li, L. Yin, Z. Chen, K. Deng, S. Luo, B. Zou, Z. Wang, J. Tang, and Z. Quan, Inorg. Chem. **58**, 1621 (2019)

[20] M. Szafranski and A. Katrusiak, J. Phys. Chem. Lett. **7**, 3458 (2016)

[21] T. Geng, Z. Ma, Y. Chen, Y. Cao, P. Lv, N. Li, and G. Xiao, Nanoscale **12**, 1425 (2020)

[22] H. K. Mao, J. A. Xu, and P. M. Bell, J. Geophys. Res. Solid Earth **91**, 4673 (1986).

[23] A. Dewaele, M. Torrent, P. Loubeyre, and M. Mezouar, Phys. Rev. B **78**, 104102 (2008).

[24] C. Preschera and V. B. Prakapenkaa, High Press. Res. **35**, 223 (2015).

[25] R. Shirley, *The CRYSFIRE 2002 System for Automatic Powder Indexing: Users Manual* (The Lattice Press, Guildford, 2002).

[26] B. H. Toby, J. Appl. Crystallogr. **34**, 210 (2001).

[27] K. Momma and F. Izumi, J. Appl. Crystallogr. **41**, 653 (2008).

[28] P. Giannozzi, S. Baroni, N. Bonini, M. Calandra, R. Car, C. Cavazzoni, D. Ceresoli, G. L. Chiarotti, M. Cococcioni, I. Dabo *et al.*, J. Phys.: Condens. Matter **21**, 395502 (2009)

[29] P. Giannozzi, O. Andreussi, T. Brumme, O. Bunau, M. B. Nardelli, M. Calandra, R. Car, C. Cavazzoni, D. Ceresoli, M. Cococcioni *et al.*, J. Phys.: Condens. Matter **29**, 465901 (2017)

[30] D. Vanderbilt, Phys. Rev. B **41**, 7892(R) (1990)

[31] J. P. Perdew, K. Burke, and M. Ernzerhof, Phys. Rev. Lett. **77**, 3865 (1996)

[32] H. J. Monkhorst and J. D. Pack, Phys. Rev. B **13**, 5188 (1976)

[33] S. Baroni, S. D. Gironcoli, A. D. Corso, and P. Giannozzi, Rev. Mod. Phys. **73**, 515 (2001)

[34] R. M. Wentzcovitch, Phys. Rev. B **44**, 2358 (1991)

[35] R. M. Wentzcovitch, J. L. Martins, and G. D. Price, Phys. Rev. Lett. **70**, 3947 (1993)

[36] F. Lazarini, Acta Crystallogr., Sect. B: Struct. Crystallogr. Cryst. Chem. **33**, 2961 (1977)

[37] E. Yu. Peresh, V. I. Sidei, O. V. Zubaka, and I. P. Stercho, Inorg. Mater. **47**, 208 (2011)

[38] T. Schmidt, K. Lischka, and W. Zulehner, Phys. Rev. B **45**, 8989 (1992)

[39] See Supplemental Material at http://link.aps.org/supplemental/10.1103/PhysRevB.105.104103 for additional figures in support of the data analysis.

[40] S. Li, J. Luo, J. Liu, and J. Tang, J. Phys. Chem. Lett. **10**, 1999 (2019)

[41] A. Pawbake, C. Bellin, L. Paulatto, K. Beneut, J. Biscaras, C. Narayana, D. J. Late, and A. Shukla, Phys. Rev. Lett. **122**, 145701 (2019)

[42] V. Rajaji, K. Pal, S. Ch. Sarma, B. Joseph, S. C. Peter, U. V. Waghmare, and C. Narayana, Phys. Rev. B **97**, 155158 (2018)

[43] M. G. Brik, G. A. Kumar, and D. K. Sardar, Mater. Chem. Phys. **136**, 90 (2012)

[44] A. Khein, D. J. Singh, and C. J. Umrigar, Phys. Rev. B **51**, 4105 (1995)

[45] I. H. Lee and R. M. Martin, Phys. Rev. B **56**, 7197 (1997)

[46] D. Liu, W. W. Lei, B. Zou, S. D. Yu, J. Hao, K. Wang, B. B. Liu, Q. L. Cui, and G. T. Zou, J. Appl. Phys. **104**, 083506 (2008)

[47] P. Borlido, J. Schmidt, A. W. Huran, F. Tran, M. A. L. Marques, and S. Botti, npj Comput. Mater. **6**, 96 (2020)

[48] Y. L. Liu, C. L. Yang, M. S. Wang, X. G. Ma, and Y. G. Yi, J. Mater. Sci. **54**, 4732 (2019)

[49] A. Koliogiorgos, S. Baskoutas, and I. Galanakis, Comput. Condens. Matter. **14**, 161 (2018)

[50] K. Saha, K. Legare, and I. Garate, Phys. Rev. Lett. **115**, 176405 (2015)

[51] S. N. Gupta, A. Singh, K. Pal, B. Chakraborty, D. V. S. Muthu, U. V. Waghmare, and A. K. Sood, Phys. Rev. B **96**, 094104 (2017)

[52] J. Shi, H. Zhang, Y. Li, J. J. Jasieniak, Y. Li, H. Wu, Y. Luo, D. Li, and Q. Meng, Energy Environ. Sci. **11**, 1460 (2018)

[53] A. Zilli, M. D. Luca, D. Tedeschi, H. A. Fonseka, A. Miriametro, H. H. Tan, C. Jagadish, M. Capizzi, and A. Polimeni, ACS Nano **9**, 4277 (2015)

[54] L. Zhang, Y. Fang, L. Sui, J. Yan, K. Wang, K. Yuan, W. L. Mao, and B. Zou, ACS Energy Lett. **4**, 2975 (2019)

[55] K. M. McCall, C. C. Stoumpos, S. S. Kostina, M. G. Kanatzidis, and B. W. Wessels, Chem. Mater. **29**, 4129 (2017)